Tunable azimuthally non-uniform orbital angular momentum carried by vector optical fields

Yue Pan (潘 岳)[1,*], Xu-Zhen Gao (高旭珍)[1], Rende Ma (马任德)[1], Chenghou Tu (涂成厚)[2], Yongnan Li (李勇男)[2], and Hui-Tian Wang (王慧田)[3,]**

[1]*School of Physics and Physical Engineering, Shandong Provincial Key Laboratory of Laser Polarization and Information Technology, Qufu Normal University, Qufu 273165, China*

[2]*School of Physics and Key Laboratory of Weak-Light Nonlinear Photonics, Nankai University, Tianjin 300071, China*

[3]*National Laboratory of Solid State Microstructures, School of Physics and Collaborative Innovation Center of Advanced Microstructures, Nanjing University, Nanjing 210093, China*

**Corresponding author: panyue.89@163.com; **corresponding author: htwang@nju.edu.cn*

Received May 30, 2020; accepted September 4, 2020; posted online October 28, 2020

Orbital angular momentum (OAM), as a fundamental parameter of a photon, has attracted great attention in recent years. Although various properties and applications have been developed by modulating the OAM of photons, there is rare research about the non-uniform OAM. We propose and generate a new kind of continuously tunable azimuthally non-uniform OAM for the first time, to the best of our knowledge, which is carried by a hybridly polarized vector optical field with a cylindrically symmetric intensity profile and a complex polarization singularity. We also present the perfect vector optical field carrying non-uniform OAM with a fixed radius independent of topological charges, which can propagate steadily without radial separation, solving the problem of the unsteady propagation due to the broadened OAM spectrum of the non-uniform OAM. This new kind of tunable non-uniform OAM with a cylindrical symmetric intensity profile, complex polarization singularity, and propagation stability enriches the family of OAMs and can be widely used in many regions such as optical manipulation, quantum optics, and optical communications.

Keywords: orbital angular momentum; vector optical field; singular optics; phase singularity; polarization singularity.

doi: 10.3788/COL202018.122601.

Light can carry both spin angular momentum (SAM) and orbital angular momentum (OAM), which are associated with circular polarizations and the spiral wave front, respectively[1]. As predicted by Allen *et al.* in 1992[2], a scalar vortex field with a helical phase of $\exp(\pm im\phi)$ can carry an optical OAM of $\pm m\hbar$ per photon, where ϕ is the azimuthal angle, and m is the topological charge. The photonic OAM, as a fundamentally new optical degree of freedom[3–7], has attracted extensive attention and academic interest due to its practical and potential applications in various realms, such as quantum optics and quantum information[4,8–13], optical communications[14–19], optical trapping and manipulation[3,20], optical imaging[21], nonlinear optics[22], and astronomy[23].

Along with the wide study and application of the OAM, novel OAM different from the traditional OAM carried by the vortex field also attracts great attention[24–27]. Meanwhile, as a new kind of OAM, the azimuthally non-uniform OAM is rarely researched, which is mainly designed and generated by modulation of non-uniform intensity distributions[28–30] and cannot keep propagation stability. Recently, new kinds of azimuthally uniform OAM carried by vector optical fields (VOFs) have been proposed[25,31–33], which provide inspiration and ideas to further design the non-uniform OAM. In this work, we propose a new kind of azimuthally non-uniform OAM (ANU-OAM) carried by VOFs with a cylindrical symmetric intensity profile and a complex polarization singularity, and the OAM is arbitrarily tunable in certain intervals. The VOFs carrying this new kind of ANU-OAM are superposed by a pair of orthogonally polarized components with opposite helical phases of $\exp(\pm im\phi)$ and complementary intensity distributions. We also present the perfect VOFs carrying the ANU-OAM that can be physically realizable, which exhibit the fixed radius and propagation stability with unseparated OAMs in the radial direction.

Under the Lorentz gauge and the paraxial approximation, an optical field can be expressed as $\mathbf{E} = i\omega\mathbf{A} + i(\omega/k^2)\nabla(\nabla\cdot\mathbf{A}) = [\mathbf{E}_T + (i/k)(\nabla\cdot\mathbf{E}_T)\hat{\mathbf{e}}_z]\exp(ikz - i\omega t)$, where $\mathbf{A}$ is the vector potential, and $\mathbf{E}_T = U(\alpha\mathbf{v}_\alpha + \beta\mathbf{v}_\beta)\exp(ikz)$ is the transverse electric field. U is the amplitude of the optical field, and the unit vector $\alpha\mathbf{v}_\alpha + \beta\mathbf{v}_\beta$ describes the distribution of state of polarization (SoP) of $\mathbf{E}$, with the restriction of $|\alpha|^2 + |\beta|^2 = 1$. $\mathbf{v}_\alpha$ and $\mathbf{v}_\beta$ are a pair of unit vectors with the orthogonal polarizations represented by any pair of antipodal points on the Poincaré sphere[34]. In this case, the OAM per photon associated with the azimuthally variant SoP is[25]

$$L_z^{(2)} = \hbar\mathrm{Im}\left(\alpha^*\frac{\partial\alpha}{\partial\phi} + \beta^*\frac{\partial\beta}{\partial\phi}\right). \tag{1}$$

We should state that we choose this equation to calculate the OAM because the optical field we would study is VOF

with azimuthally variant SoP. In addition, there are other equations to calculate OAM corresponding to the azimuthally variant phase distribution and radially variant polarization distribution, which we will not discuss in detail.

To achieve the ANU-OAM with a cylindrical symmetric intensity profile, let us refocus on the azimuthally varying hybridly polarized VOF[34], whose two orthogonally polarized components carry the opposite helical phases and the same uniform intensities profiles. This brings us an inspiration that if the intensie of two orthogonally polarized components are complementary instead of azimuthally uniform, what would the OAM carried by the VOFs be? We consider the case where the incident transverse VOFs can be represented as

$$\mathbf{E}_T = [U_{\mathrm{A}}(\phi)e^{im\phi}\hat{\mathbf{e}}_x + U_{\mathrm{B}}(\phi)e^{-im\phi}\hat{\mathbf{e}}_y]e^{ikz}, \tag{2}$$

where $U_{\mathrm{A}}(\phi)$ and $U_{\mathrm{B}}(\phi)$ are functions of ϕ, and $|U_{\mathrm{A}}(\phi)|^2 + |U_{\mathrm{B}}(\phi)|^2 = 1$, meaning that the total intensiy is azimuthally invariant. The pair of unit vectors is chosen to be linearly polarized unit vectors $(\hat{\mathbf{e}}_x, \hat{\mathbf{e}}_y)$ in this work without losing generality. The two components $U_{\mathrm{A}}(\phi)e^{im\phi}\hat{\mathbf{e}}_x$ and $U_{\mathrm{B}}(\phi)e^{-im\phi}\hat{\mathbf{e}}_y$ are the +1st and −1st-order diffractions from the holographic grating used in experiment. These two orders are two components of the VOF, which can be experimentally measured separately. It should be pointed out that though designing VOFs with the superposition of a pair of orthogonal vector bases carrying opposite optical vortices is a common method[31–34], this is the first time, to the best of our knowledge, to superpose the two bases with azimuthally nonuniform intensity distributions to design the OAM. In this case, the average OAM per photon should be

$$L_z^{(2)} = \hbar \mathrm{Im}\left(\alpha^* \frac{\partial \alpha}{\partial \phi} + \beta^* \frac{\partial \beta}{\partial \phi}\right) = m\hbar[2|U_{\mathrm{A}}(\phi)|^2 - 1], \tag{3}$$

which indicates that the OAM has a range of $[m\hbar[2|U_{\mathrm{A}}(\phi)|^2_{\min} - 1], m\hbar[2|U_{\mathrm{A}}(\phi)|^2_{\max} - 1]]$ and is arbitrarily changable within $[-m\hbar, m\hbar]$. For simplicity, here we take $U_{\mathrm{A}}(\phi)$ and $U_{\mathrm{B}}(\phi)$ as

$$U_{\mathrm{A}}(\phi) = \frac{1}{\sqrt{a+b+1}}\sqrt{a + \cos^2(n\phi)}, \tag{4a}$$

$$U_{\mathrm{B}}(\phi) = \frac{1}{\sqrt{a+b+1}}\sqrt{b + \sin^2(n\phi)}, \tag{4b}$$

where a and b are non-negative numbers controlling the range, and the OAM per photon can be writtern as

$$L_z^{(2)} = m\hbar\frac{a - b + \cos(2n\phi)}{a+b+1}, \tag{5}$$

meaning that the OAM has a range of $[m\hbar(a-b-1)/(a+b+1), m\hbar(a-b+1)/(a+b+1)]$ and can be controlled by the parameters a and b within the maximum change range of $[-m\hbar, +m\hbar]$. For instance, when $(a, b) = (0, 0)$, $L_z^{(2)}$ is $m\hbar\cos(2n\phi)$ with a range of $[-m\hbar, m\hbar]$; when $a = 3/5$ and $b = 4/5$, the change range of the OAM is $[-m\hbar/2, m\hbar/3]$.

Figure 1 shows the scheme of generating the VOF carrying ANU-OAM with $(a, b) = (0, 0)$ and $(m, n) = (2, 2)$. Figure 1(a) shows the intensity and phase of the +1st order of $|\cos(2\phi)|e^{i2\phi}\hat{\mathbf{e}}_x$, where the blue arrows indicate the direction of the energy flow induced by the OAM. The green and gray-scale patterns represent the intensity and phase distributions of the optical fields, respectively. Figure 1(c) shows the intensity and phase of the −1st order of $|\sin(2\phi)|e^{-i2\phi}\hat{\mathbf{e}}_y$. The intensity modulated OAMs per photon corresponding to the two orders are depicted in Figs. 1(b) and 1(d), respectively. Obviously, the intensity distributions of the two orders are azimuthally nonuniform and complementary. As a result, the intensity of the VOF, which is generated by superposing the two orders, is azimuthally uniform, as shown in Fig. 1(e). We also find that the VOF we design is in fact hybridly polarized with linear and elliptic polarizations in the wavefront of the field simultaneously. The OAM per photon of the VOF changes from $-2\hbar$ to $2\hbar$ with a period of $\pi/2$, as shown in Fig. 1(f). Obviously, we can find from the above discussion that the ANU-OAM carried by the VOF with a cylindrical symmetric intensity profile can be generated in this superposing method. Moreover, we can see from Fig. 1(e) that a singularity of polarization exists at the center of the total intensity pattern. As is well known, the polarization singularity has attracted interest in recent years[35–40]. The V-point is defined as the point where the direction of the linear polarization vector is undefined at the beam center, and the C-point is the isolated point of circular polarization, where the orientation of the major axis of polarization ellipse is undefined. The L-line (line of linear polarization) is where the handedness of linear polarization is undefined. The polarizations around

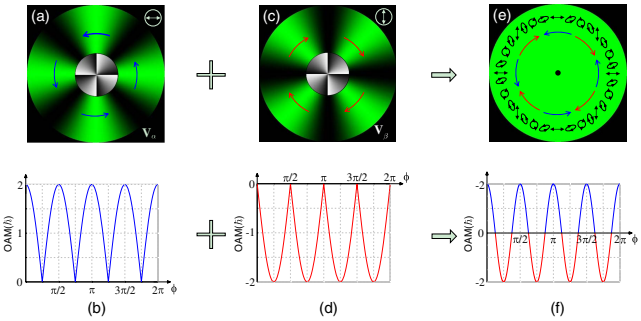

Fig. 1. Scheme of the ANU-OAM with $(a, b) = (0, 0)$ and $(m, n) = (2, 2)$. (a), (c), and (e) The intensity, phase, polarization, and energy flow direction for the +1st order, −1st order, and the superposed VOF, respectively. (b) and (d) Dependence of the intensity modulated OAM per photon on the azimuthal coordinate ϕ for the ±1st orders. (f) Dependence of the average OAM per photon on the azimuthal coordinate for the superposed VOF. The blue and red arrows represent the directions of the energy flow, and the white arrows represent the polarization directions. The green and gray-scale patterns represent the intensity and phase distributions of the optical fields, respectively.

this point contain linear, elliptical, and circular polarizations, which lead to the results that this point is not in accordance with any named singularity. Thus, we call this singularity a complex singularity, where the orientation, ellipticity, and handedness of the polarization are all uncertain simultaneously, and this kind of singularity already exists in the VOF with hybrid SoP[34,39]. Compared with the phase singularity at the center of the vortex field, the complex singularity of the ANU-OAM we design is an obvious feature that is different from the traditional OAM.

The experimental setup for generating the VOFs carrying ANU-OAM is shown in Fig. 2(a), which is a common-path interferometric configuration with the aid of a $4f$ system composed of two lenses, similar to Refs. [41,42]. The linearly polarized light delivered from a laser (Verdi-5, Coherent Inc.) is incident on the spatial light modulator (SLM, Pluto-Vis, Holoeye System Inc.) with 1920×1024 pixels (each pixel has a dimension of $8\ \mu\text{m} \times 8\ \mu\text{m}$). The two-dimensional holographic grating in the inset of Fig. 2(a) is loaded on the SLM and then diffracts the input light. The $+1$st order in the x direction and the -1st order in the y direction are chosen and then converted into the horizontal and vertical polarized fields by two 1/2 wave plates located at the Fourier plane of the $4f$ system, respectively. The two orthogonally polarized orders of $U_{\text{A}}(\phi)e^{im\phi}\hat{\mathbf{e}}_x$ and $U_{\text{B}}(\phi)e^{-im\phi}\hat{\mathbf{e}}_y$ are recombined by the Ronchi phase grating placed in the output plane of the $4f$ system. The interference setup shown in Fig. 2(b) is used to measure the interference patterns between the ± 1 orders and the reference beam.

Figure 3 shows the VOFs carrying ANU-OAM with $(a, b) = (0, 0)$ and $(m, n) = (2, 2)$. The total intensity and the simulated SoP distribution of the VOF are shown in Fig. 3(a). A zero-intensity dark spot exists in the center of the field due to the complex singularity the VOF carries. The interference pattern between the $+1$st (-1st) order and the horizontally (vertically) polarized reference beam is shown in Fig. 3(b) [Fig. 3(c)]. The forked shape in the interference pattern indicates the topological charge $(m = 2)$ embedded in ± 1st orders of the generated VOF. Furthermore, the number of sector-shaped half-extinctions in the interference pattern is equal to $2n$. Thus, the OAM of the VOF generated by the superposition of the ± 1st orders can be determined by $L_z^{(2)} = 2\hbar\cos(4\phi)$ with a change range of $[-2\hbar, 2\hbar]$. The experimentally measured Stokes parameters shown in the second row of Fig. 3 are in good agreement with the simulated results shown in the insets. As the Stokes parameter S_3 shown in Fig. 3(f), the ellipticity of polarization is azimuthally variant, which illustrates that the generated field is a hybridly polarized VOF.

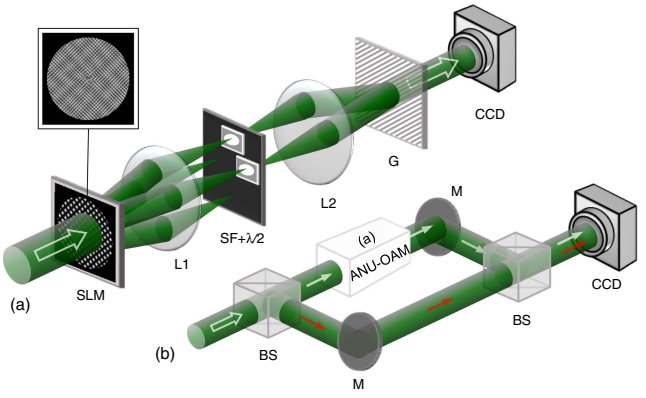

Fig. 2. Schematic of the experimental setup for generating and measuring the desired VOFs carrying ANU-OAM. (a) The generating setup. SLM, spatial light modulator; L1 ($f = 300\,\text{mm}$) and L2 ($f = 200\,\text{mm}$), a pair of lenses; $\lambda/4$, quarter-wave plate; SF, spatial filter; G, Ronchi phase grating; CCD, charge-coupled device; inset, two-dimensional holographic grating. (b) The interference setup. BS, beam splitter; M, mirror. The white cuboid in (b) represents the setup in (a).

Besides the VOF carrying ANU-OAM with a cylindrical symmetric intensity profile, the ± 1st orders of the VOF can also carry ANU-OAM, which is shown in Figs. 1(b) and 1(d) as the intensity modulated OAM. In fact, a kind of fractional OAM[28,29] is also ANU-OAM with the ANU intensity distribution. However, as a combination of a series of weighted integer OAMs, the ANU-OAM controlled by ANU intensity distribution will in general undergo a separation in radial direction during propagation. In order to gain insights into this phenomenon, we numerically simulate the OAM spectrum of the $+1$st order with $(a, b) = (0, 0)$ and $(m, n) = (4, 2)$ by the Fourier transform[43,44]

$$U_l = \frac{1}{2\pi}\int_{-\pi}^{\pi} U_{\text{A}}(\phi)e^{im\phi}e^{-il\phi}\text{d}\phi. \tag{6}$$

The numerically simulated OAM spectrum $|U_l|^2$ of the $+1$st order for $U_{\text{A}}(\phi) = |\cos(2\phi)|$ is shown in Fig. 4(a).

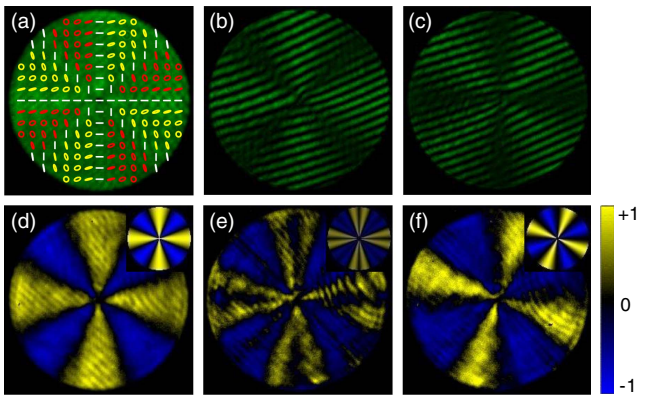

Fig. 3. VOFs carrying ANU-OAM with $(a, b) = (0, 0)$ and $(m, n) = (2, 2)$. (a) The total intensity pattern and the simulated SoP distribution with linear (white), left-handed (red), and right-handed (yellow) polarizations, respectively. (b) The interference pattern between the $+1$st order and the horizontally polarized reference beam. (c) The interference pattern between the -1st order and the vertically polarized reference beam. The measured Stokes parameters of (d) S_1, (e) S_2, and (f) S_3 are shown in the second row. The corresponding simulated Stokes parameters are shown in the insets, respectively.

We can see that the OAM is broadened to three primary angular momentum states as 0, $4\hbar$, and $8\hbar$, respectively. The relative weights of the OAMs of $4\hbar$ and 0 are 0.407:0.046. As a contrast, the simulated OAM spectrum of the optical field with $U_{\mathrm{A}}(\phi) = \cos(2\phi)$ is shown in Fig. 4(b). The OAM spectrum has two sidebands of $2\hbar$ and $6\hbar$, which have the relative weights of 0.25 normalized by the maximum intensity of the initial mode. The traditional ANU-OAM carried by the vortex field with ANU intensity can be expressed as a series of weighted integer OAMs. As a result, the ANU-OAM modulated by intensity cannot propagate steadily and will separate in the radial direction during propagation. Meanwhile, as the superposition of two vortex fields with complementary intensity distributions, the VOF carrying ANU-OAM we presented cannot propagate steadily, because it is the superposition of a series of eigenmodes of the paraxial wave equation.

To overcome the above-mentioned drawback of propagation instability, we introduce the concept of the perfect vortex beam to create the VOFs carrying ANU-OAM. Here, we design and generate the perfect VOFs carrying ANU-OAM, whose cylindrical symmetric intensity profile is independent of the topological charges (m, n) within a certain propagation distance. To generate the perfect VOFs carrying ANU-OAM, we combine techniques for generation of perfect vortex beams[45–47] with the methods of generating the arbitrary VOFs[41,42]. In experiment, a two-dimensional holographic grating with an axicon phase is encoded on an SLM to generate the Bessel–Gaussian VOF. Then, a convex lens can realize the transformation from the Bessel–Gaussian VOF into the perfect VOF. Figure 5 shows the perfect VOFs carrying ANU-OAM with $m = 1, 2, 3$ and $n = 1, 2$, which illustrates that the ring radius of the perfect VOFs remains a constant of ~0.47 mm for different values of (m, n). That is to say, the diameters of the perfect VOFs are independent of the parameters m and n.

We further explore the dependence of the radius of the generated perfect VOFs carrying ANU-OAM with $(m, n) = (1, 2)$, $(2, 1)$, and $(5, 2)$ on the propagation distance z, as shown in Fig. 6. We define the $z = 0$ plane as the focal plane of the lens, which is used to implement the Fourier transform of the Bessel–Gaussian VOF for

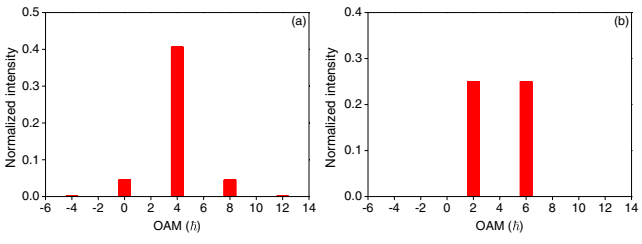

Fig. 4. Numerically simulated OAM spectra of two vortex optical fields with non-uniform amplitude profiles expressed as (a) $|\cos(2\phi)|e^{i4\phi}\mathbf{v}_\alpha$ and (b) $\cos(2\phi)e^{i4\phi}\mathbf{v}_\alpha$, respectively. The spectral intensities are normalized by the maximum intensity of the initial mode.

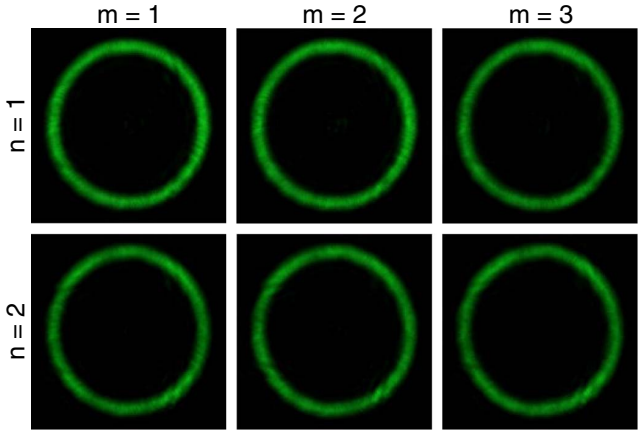

Fig. 5. Intensity of the perfect VOFs carrying ANU-OAM with $m = 1, 2, 3$ and $n = 1, 2$. All of the pictures have the same size of 1.2 mm × 1.2 mm.

generating the perfect VOF. As the propagation distance increases, the radius of the perfect VOF gradually decreases from ~0.55 to ~0.4 mm. However, the three VOFs have approximately the same radius at the same propagation distance z, meaning that the radius of the perfect VOF we generated is independent of the topological charge (m, n). The most important advantage of the perfect VOFs carrying ANU-OAM is that in our method the ±1st orders do not separate during propagation, implying that the ANU-OAM we generated can propagate steadily within a distance of ~100 mm, which is much longer than the depth of focus of the focal lens used in the experiment ($2\lambda/\mathrm{NA}^2 \approx 10$ mm).

In summary, we propose a new kind of ANU-OAM carried by the VOFs for the first time, to the best of our knowledge. We design and generate the VOFs by superposing two orders of vortex optical fields with complementary intensity distributions. Meanwhile, we show the Stokes parameters of the VOFs and measure the intensity and interference patterns of the two orders. To overcome

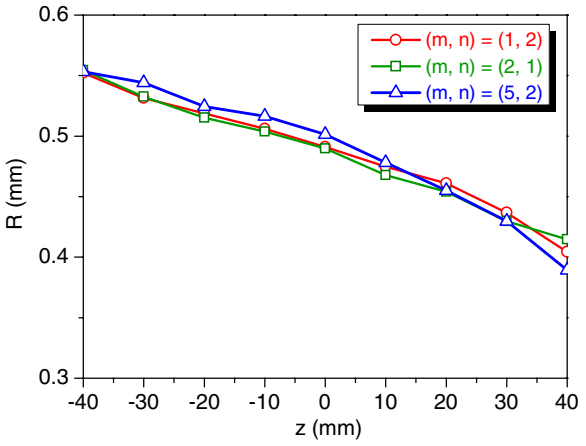

Fig. 6. Dependence of the radius R of the experimentally generated perfect VOFs carrying ANU-OAM with $(m, n) = (1, 2)$, $(2, 1)$, and $(5, 2)$ on the propagation distance z within a propagation range of $z \in [-40, 40]$ mm.

the drawback of propagation instability, the perfect VOFs carrying ANU-OAM are experimentally generated. The ANU-OAM we propose has novel and unique natures: (i) it is azimuthally tunable within the arbitrary range of $[-m\hbar, m\hbar]$, (ii) it has the cylindrical symmetric intensity profile and a complex polarization singularity, (iii) the radius of the perfect VOF carrying ANU-OAM is independent of the topological charges, and (iv) the perfect VOF retains the stability without radial separation of the OAM during propagation. These novel properties can guarantee steady non-uniform OAM in space, which can be applied in realms such as optical manipulation, quantum optics, and optical communications. In addition, this new kind of ANU-OAM carried by the VOFs enriches the family of OAMs.

This work was supported by the National Natural Science Foundation of China (Nos. 11534006, 11804187, 11904199, 11674184, and 11774183), Natural Science Foundation of Shandong Province (No. ZR2019BF006), Shandong Province Higher Educational Science and Technology Program (No. J18KA229), and Collaborative Innovation Center of Extreme Optics.

References

1. M. Padgett, Phys. Today **35**, 57 (2004).
2. L. Allen, M. W. Beijersbergen, R. J. C. Spreeuw, and J. P. Woerdman, Phys. Rev. A **45**, 8185 (1992).
3. D. G. Grier, Nature **424**, 810 (2003).
4. G. Molina-Terriza, J. P. Torres, and L. Torner, Nat. Phys. **3**, 305 (2007).
5. Y. Shen, X. Wang, Z. Xie, C. Min, X. Fu, Q. Liu, M. Gong, and X. C. Yuan, Light Sci. Appl. **8**, 90 (2019).
6. Z. X. Wang, Y. C. Xie, S. Y. Huang, H. Zhou, R. Liu, Z. F. Liu, M. Wang, W. R. Qi, Q. Q. Tian, L. J. Kong, C. H. Tu, Y. N. Li, and H. T. Wang, Chin. Opt. Lett. **17**, 120601 (2019).
7. S. S. Liu, X. D. Chen, J. X. Pu, Z. L. Lin, and Z. Y. Chen, Chin. Phys. Lett. **36**, 124203 (2019).
8. A. Mair, A. Vaziri, G. Weihs, and A. Zeilinger, Nature **412**, 313 (2001).
9. X. L. Wang, X. D. Cai, Z. E. Su, M. C. Chen, D. Wu, L. Li, N. L. Liu, C. Y. Lu, and J. W. Pan, Nature **518**, 516 (2015).
10. D. S. Ding, W. Zhang, Z. Y. Zhou, S. Shi, G. Y. Xiang, X. S. Wang, Y. K. Jiang, B. S. Shi, and G. C. Guo, Phys. Rev. Lett. **114**, 050502 (2015).
11. X. W. Luo, X. Zhou, J. S. Xu, C. F. Li, G. C. Guo, C. W. Zhang, and Z. W. Zhou, Nat. Commun. **8**, 16097 (2017).
12. G. Y. Zhu, L. Xiao, B. Z. Huo, and P. Xue, Chin. Opt. Lett. **18**, 052701 (2020).
13. L. J. Kong, R. Liu, W. R. Qi, Z. X. Wang, S. Y. Huang, C. H. Tu, Y. N. Li, and H. T. Wang, Chin. Phys. Lett. **37**, 034204 (2020).
14. J. Wang, J. Y. Yang, I. M. Fazal, N. Ahmed, Y. Yan, H. Huang, Y. X. Ren, Y. Yue, S. Dolinar, M. Tur, and A. E. Willner, Nat. Photon. **6**, 488 (2012).
15. N. Bozinovic, Y. Yue, Y. Ren, M. Tur, P. Kristensen, H. Huang, A. E. Willner, and S. Ramachandran, Science **340**, 1545 (2013).
16. N. B. Zhao, X. Y. Li, G. F. Li, and J. M. Kahn, Nat. Photon. **9**, 822 (2015).
17. T. Lei, M. Zhang, Y. R. Li, P. Jia, G. N. Liu, X. G. Xu, Z. H. Li, C. J. Min, J. Lin, C. Y. Yu, H. B. Niu, and X. C. Yuan, Light Sci. Appl. **4**, e257 (2015).
18. S. Wei, D. Wang, J. Lin, and X. Yuan, Opto-Electron. Adv. **1**, 18000601 (2018).
19. S. Y. Fu, Y. W. Zhai, H. Zhou, J. Q. Zhang, C. Yin, and C. Q. Gao, Chin. Opt. Lett. **17**, 080602 (2019).
20. A. C. Ji, W. M. Liu, J. L. Song, and F. Zhou, Phys. Rev. Lett. **101**, 010402 (2008).
21. L. X. Chen, J. J. Lei, and J. Romero, Light Sci. Appl. **3**, e153 (2014).
22. D. N. Neshev, T. J. Alexander, E. A. Ostrovskaya, Y. S. Kivshar, H. Martin, I. Makasyuk, and Z. G. Chen, Phys. Rev. Lett. **92**, 123903 (2004).
23. G. C. G. Berkhout and M. W. Beijersbergen, Phys. Rev. Lett. **101**, 100801 (2008).
24. J. Leach, E. Yao, and M. J. Padgett, New. J. Phys. **6**, 71 (2004).
25. X. L. Wang, J. Chen, Y. N. Li, J. P. Ding, C. S. Guo, and H. T. Wang, Phys. Rev. Lett. **105**, 253602 (2010).
26. A. Chong, C. Wan, J. Chen, and Q. Zhan, Nat. Photon. **14**, 350 (2020).
27. Z. Man, Z. Xi, X. Yuan, R. E. Burge, and H. P. Urbach, Phys. Rev. Lett. **124**, 103901 (2020).
28. V. V. Kotlyar, A. A. Kovalev, R. V. Skidanov, and V. A. Soifer, J. Opt. Soc. Am. A **31**, 1977 (2014).
29. V. V. Kotlyar, A. A. Kovalev, and A. P. Porfirev, Opt. Lett. **42**, 139 (2017).
30. X. Z. Li, H. Ma, C. Yin, J. Tang, H. Li, M. Tang, J. Wang, Y. Tai, X. Li, and Y. Wang, Opt. Express **26**, 651 (2018).
31. G. Milione, H. I. Sztul, D. A. Nolan, and R. R. Alfano, Phys. Rev. Lett. **107**, 053601 (2011).
32. G. Milione, S. Evans, D. A. Nolan, and R. R. Alfano, Phys. Rev. Lett. **108**, 190401 (2012).
33. Y. Pan, X. Z. Gao, Z. C. Ren, X. L. Wang, C. H. Tu, Y. N. Li, and H. T. Wang, Sci. Rep. **6**, 29212 (2016).
34. X. L. Wang, Y. N. Li, J. Chen, C. S. Guo, J. P. Ding, and H. T. Wang, Opt. Express **18**, 10786 (2010).
35. I. Freund, Opt. Commun. **201**, 251 (2002).
36. R. Schoonover and T. Visser, Opt. Express **14**, 5733 (2006).
37. M. Dennis, Opt. Commun. **213**, 201 (2002).
38. I. Freund, M. S. Soskin, and A. I. Mokhun, Opt. Commun. **208**, 223 (2002).
39. G. M. Lerman, L. Stern, and U. Levy, Opt. Express **18**, 27650 (2010).
40. E. Otte, C. Schlickriede, C. Alpmann, and C. Denz, Proc. SPIE **9379**, 937908 (2015).
41. Z. Yu, H. Chen, Z. Chen, J. Hao, and J. P. Ding, Opt. Commun. **345**, 135 (2015).
42. Z. Chen, T. Zeng, B. Qian, and J. P. Ding, Opt. Express **23**, 17701 (2015).
43. S. Franke-Arnold, S. M. Barnett, E. Yao, J. Leach, J. Courtial, and M. Padgett, New J. Phys. **6**, 103 (2004).
44. B. Jack, M. J. Padgett, and S. Franke-Arnold, New J. Phys. **10**, 103013 (2008).
45. P. Vaity and L. Rusch, Opt. Lett. **40**, 597 (2015).
46. S. Fu, T. Wang, and C. Gao, J. Opt. Soc. Am. A. **33**, 1836 (2016).
47. X. Li, H. Ma, C. Yin, J. Tang, H. Li, M. Tang, J. Wang, Y. Tai, X. Li, and Y. Wang, Opt. Express **26**, 651 (2018).